Available online at www.sciencedirect.com
ScienceDirect
Trans. Nonferrous Met. Soc. China 29(2019) 893−906

Transactions of
Nonferrous Metals
Society of China
www.tnmsc.cn

Impact of Zener-Hollomon parameter on substructure and texture evolution during thermomechanical treatment of iron-containing wrought aluminium alloys

Evgenii ARYSHENSKII[1,2], Jürgen HIRSCH[2,3], Vladimir BAZHIN[4], Rudolf KAWALLA[1], Ulrich PRAL[1]

1. TU Bergakademie Freiberg, Institut für Metallformung, Bernhard-von-Cotta-Str. 4, 09599 Freiberg, Germany;
2. Samara State Aerospace University, Samara National Research University,
MoskovskoyeShosse 34, 443086 Samara, Russia;
3. Hydro Aluminium Rolled Products GmbH, Research and Development, D-53117 Bonn, Germany;
4. St. Petersburg Mining University, Institute of Automation of Manufacturing Processes,
2, 21st Line, St Petersburg 199106, Russia

Received 20 August 2018; accepted 27 March 2019

Abstract: The objective of the investigation is to evaluate the influence of the Zener-Hollomon parameter on substructure and texture evolution in iron-containing wrought aluminium alloys (type AA8011). Methods applied are X-ray texture analysis, electron backscatter diffraction (EBSD) and optical microscopy. The results show a serious impact of the Zener-Hollomon parameter on cube texture evolution during the thermomechanical treatment in iron-containing aluminium alloys. An increase in the Zener-Hollomon parameter reduces the survivability of cube texture during hot deformation and reinforces particle-stimulated nucleation (PSN) during the annealing process. However, thermomechanical treatment at low temperatures leads to active precipitation and as a result fine-dispersed participles tend to block all nuclei except for those producing large cube-oriented grains. It is concluded that in iron-containing wrought aluminium alloys, the general correlation between the Zener-Hollomon parameter and subgrain size is similar to that observed in 3xxx series alloys and can be described by the specific set of equations derived.

Key words: aluminium alloy; texture; Zener-Hollomon parameter; substructure; hot rolling

---

1 Introduction

Aluminium alloys are used in almost all areas of modern industry and are particularly common in the aerospace, automotive and food packaging industries [1−4], with most such aluminium products fabricated from flat-rolled sheet and strips. One key problem related to this production process is the anisotropy of mechanical properties, which is caused by the strong crystalline texture generated during the thermo-mechanical treatment of aluminium alloys. Anisotropy leads to problems in formability and strength variations and is generally tested by measuring the earing behaviour in deep drawing (Fig. 1). The anisotropy involved reduces the stability of subsequent aluminium sheet processing and further processing of parts and may ultimately contribute to inadequate properties and an increase in costs [5,6].

The most common method applied for anisotropy compensation in highly cold-rolled sheet, like cast iron billet, is to overlay cube texture components, which cause peaks at 0°/90°, by β-fiber textures, which cause opposing peaks at 45° [6−8]. To achieve the above-mentioned compensation, simulation tools which use reliable models that describe the evolution of both texture effects and structure evolution during thermo-mechanical processing of aluminum alloys are applied. For 3xxx and 5xxx group alloys, such models have been developed and tested successfully over the last two decades [9−14]. However, they are still not available for iron-rich alloys, including 8xxx group, and the first scientific works discussing structure and texture development during the complex thermomechanical treatment of these alloys were published not so long ago [15,16]. The reason is that the texture evolution of

---

Corresponding author: Jürgen HIRSCH; E-mail: juergen.hirsch@hydro.com

DOI: 10.1016/S1003-6326(19)64999-X

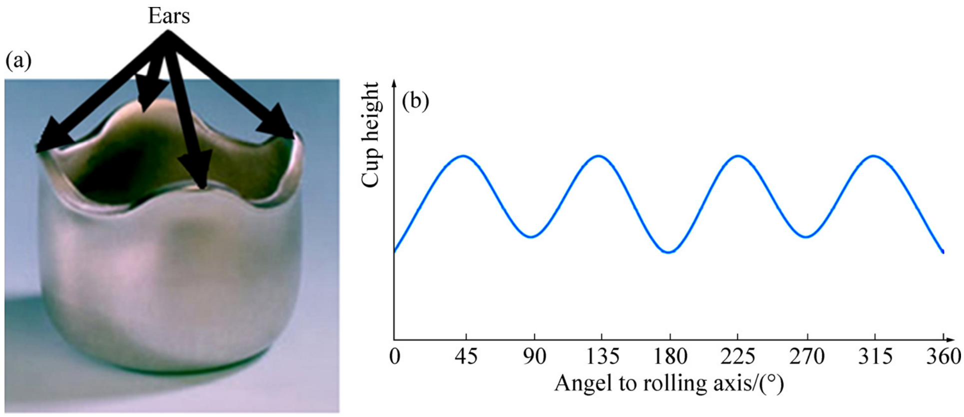

Fig. 1 Earing as main manifestation of workpiece anisotropy (a) and S texture type in aluminum alloys (b)

iron-rich aluminum alloys is different from that observed in 3xxx and 5xxx alloys due to their tendency to form sharp cube textures [15,17−20].

To provide efficient development and implementation of a model describing such texture and structure evolution during hot/cold rolling and annealing, the relationship between microstructure, subgrain size and thermomechanical parameters must be determined correctly as the subgrain type and size directly affect the texture capability for constituent nucleation [11,21−23].

Several major studies have demonstrated that during deformation and saturation (stabilization) of subgrain the structure is achieved during the hot processing. Further strain intensification has no effect on subgrain size. Furthermore, many studies have established that subgrain size has linear relationship with yield stress, while the latter is directly linked to the Zener-Hollomon (Z-H) parameter during hot deformation [24−28]. Since then, a number of equations describing the relationship between this parameter and subgrain size have been proposed and the following one is the most commonly applied [24,25,29,30]:

$$\delta_{\text{SS}}^{-m} = A + B\ln Z \tag{1}$$

Some models [23,31] also utilize the following equation:

$$\frac{1}{\delta} = \frac{kT_{\text{D}}}{A^{*}}\ln\left(\frac{Z\delta^{2}}{B^{*}}\right) \tag{2}$$

where δ_{SS} is subgrain size, Z is Zener-Hollomon parameter, m, A and B are empirically selected coefficients, and T is temperature.

In each case, Z-H parameter is as follows:

$$Z = \dot{\varepsilon}\exp\left(\frac{Q}{RT}\right) \tag{3}$$

where $\dot{\varepsilon}$ is strain rate, and Q is activation energy.

It should be noted that the relationship between the Z-H parameter and the sub-structure size is well researched for 3xxx and 1xxx series alloys [24,25,29], where increased parameter value leads to decreased size of the subgrain during various thermomechanical processes. However, although in most cases Eq. (1) has provided good results, it may not be always suitable for individual alloys at high Z-H parameter values.

It is important to note that the relationship between the Z-H parameter and subgrain size has not been studied specifically for wrought iron-rich aluminum alloys. These alloys contain a larger number of fine particles and/or a higher amount of dissolved iron and silicon compared to 3xxx and 1xxx series alloys. Such factors definitely have a strong effect on substructure development [32−36]. Therefore, the relationship between subgrain size and the Z-H parameter, as well as the applicability of Eq. (1) need to be determined for these alloys, in particular.

The Z-H parameter impact can be observed not only in terms of subgrain size but also textural evolution of alloys. It has been reported, for example in Refs. [23,37], that the opportunity for particle-simulated nucleation (PSN) in 3xxx and 5xxx series alloys increases with an increase in Z-H parameter values. Additionally, higher parameter values lead to decrease in cube texture survival [38−40] during deformation, thereby reducing its volume during recrystallization.

The presence of fine dispersed particles can seriously change the main texture component distribution. In Al alloys containing high elements or scandium additions, recrystallization after hot deformation may be completely suppressed by fine particles and grain boundary mobility retardation is caused by ambient impurity atoms [41−43]. The volume of fine dispersed participles in iron-containing aluminum alloys is less than that in aluminum−scandium alloys and higher than that in 3xxx (Al−Mn) and 5xxx (Al−Mg−Mn) series alloys [15,18,44]. As a result, although the fine particles present in wrought aluminum alloys do not fully suppress the recrystallization process, the growth of cube nuclei is stimulated more than that of other texture components. The reason for this is that cube-oriented nucleation zones are characterized by coarser subgrain structures with subgrain sizes 1.5−2 times compared to the average of other texture component nuclei [9,21,45]. Fine particles, precipitating at low temperatures, efficiently inhibit the growth of the other component nuclei which are smaller than the cube-oriented subgrains [18]. In this context, deformation involving low Z-H parameter values and further low-temperature annealing result in an increase in the cube texture fraction. In contrast, excessive cube orientation levels are not observed in alloys deformed at low Z-H parameter values and annealed at high temperatures. In this case, the distribution of the main texture components is close to the one observed in 3xxx series alloys [18].

Thus, high values of the Z-H parameter in this group of alloys may have the opposite effect on cube texture formation, increasing its volume fraction and inhibiting the growth of other components. On the other hand, such values reduce cube nuclei ‘survival’ during thermomechanical treatment. Therefore, the objective of the present research is to determine whether these alloys also exhibit correlation between the residual cube texture after deformation and the fractions formed during recrystallization, or fine particle effects prevail and the texture composition is not affected by the residual cube texture fraction after recrystallization.

An additional reason for the investigation of the abovementioned problem is that iron and manganese (used in 3xxx group) are transition elements. At the same time, addition of transition elements in aluminum alloys is a promising trend. For example, Zr and Sc additions are also very popular in modern aluminum alloys [46−48]. Comparison of data about the effect of the Z-H parameter on the substructure size (and thus new grain nuclei) for alloys with iron and manganese additives can be important. It is necessary for general understanding how transitional elements impact substructure size, recrystallization nuclei and as result the recrystallization texture.

2 Experimental

In order to investigate the effect of the Z-H parameter on the subgrain size, 8011 alloy specimens were hot rolled. The selected material is typical iron-rich wrought aluminum alloy (with its chemical composition shown in Table 1). The analyzed samples were delivered in a hot-rolled state. Rolling at different Z-H parameter values was performed in a DIMA 300 single-stand two-high reversing mill according to the schedules displayed in Table 2. The samples were water-cooled immediately after rolling for structure fixation, before being sent for structure and sub-structure analyses.

Since during the relatively short time of metal-to-roll contact the thermal influence of the roll does not reach deep into bulk of the metal, it is assumed that the average temperature T_{avg} should be closer to T_0. Therefore, $T_{\mathrm{avg}}=2/3T_0+1/3T_1$ was used instead of $T_{\mathrm{avg}}=(T_0+T_1)/2$. Under this assumption, the temperature distribution during hot rolling in distinctive workpiece layers was calculated by DEFORM 2D. The result is presented in Fig. 2.

The sample substructure was automatically analyzed using backscattered electron diffraction patterns (EBSD) obtained from TESCAN VEGA3 LMH scanning electronic microscope with $\mathrm{LaB_6}$ cathode at 20 kV and EBSD-HKLNordlys detector. The scanned area size was 80 mm × 80 mm with a 0.4 μm step, EBSD samples were prepared via the mechanical polishing method and electrolytic polishing in A2 (Struers) at 21−22 V.

The EBSD analysis detects backscattered electrons which diffract from different crystal planes and form the Kikuchi band patterns. The Kikuchi band is a pair of parallel lines, resulting from the diffraction of electrons backscattered from a specific single plane of a crystalline lattice. Diffraction from all atomic planes forms a set of

Table 1 Chemical composition of 8011 alloy (wt.%)

Component								Impurity	
Fe	Si	Mn	Mg	Zn	Ti	Cu	Cr	Each	Sum
0.7–0.8	0.7–0.8	0.05	0.02–0.08	0.05	0.05	0.03–0.06	0.03	≤0.05	≤0.15

Table 2 Single-stand hot rolling mill schedules and corresponding Z-H parameter values

Sample No.	Initial thickness/ mm	Final thickness/ mm	Roll linear speed/ $(\mathrm{m\cdot min^{-1}})$	Rolling entry temperature/ °C	Rolling exit temperature/ °C	Deformation temperature/ °C	Strain rate/$\mathrm{s^{-1}}$	Z-H parameter
1	10	4.7	15	480	300	420	5.00	1.03×10^{12}
2	10	4.7	15	380	253	338	5.00	3.44×10^{13}
3	10	4.7	15	250	197	232	5.00	1.63×10^{16}

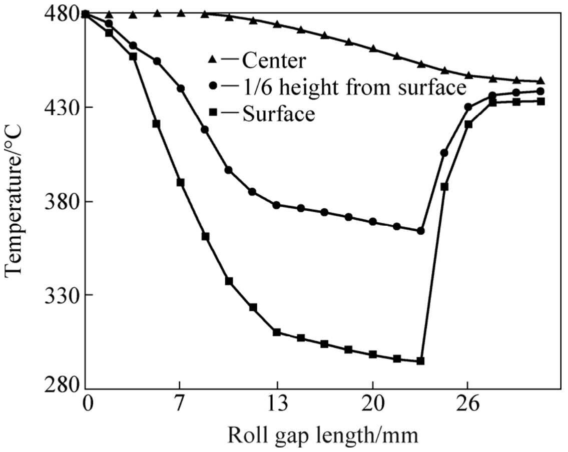

Fig. 2 Result of temperature distribution calculation during hot rolling in distinctive workpiece layers

Kikuchi bands, referred to as the diffraction pattern detected in the phosphorous screen. For indexing each pattern, five Kikuchi bands were used.

To further enhance the reliability and accuracy of EBSD data: 1) fine grains consisting of only two or one pixel were excluded from the analysis using standard TSL software, 2) all grain borders with misorientation more than 15° were taken into account as high angle boundaries, and 3) all fine grain boundaries with the angle lower than 2° were excluded from analysis.

The mean angular deviation (MAD) was applied for automatic indexing and ranking of solutions, where MAD value below 1 represents a good agreement. In this study, MAD coefficient <1 was applied.

It was also taken into account that the samples, when being rolled in the laboratory mill, would always cool rapidly during the deformation process, as seen in Table 2. It is almost impossible to achieve isothermal conditions during hot rolling in a single-stand laboratory mill, mostly because of the inter-deformation intervals (which are unavoidable for total reduction values exceeding 40%). In order to overcome this difficulty, rolling was also carried out using a continuous multi-stand mill. Thus, to check the effect of Z-H parameter on the cube texture fraction, additional experiments were conducted using the commercial four-stand continuous hot rolling mill. Rolling was performed based on four rolling schedules, presented in Table 3.

The first rolling schedule was executed at high temperature and high strain rate level in all stands; in this case, the value of the Z-H parameter was fairly low. In the second schedule, rolling was performed at a high Z-H parameter value, based on a low speed that stimulated rapid cooling and low temperatures. These two schedules were selected in order to establish how the cube texture is preserved during deformation under different Z-H parameter values. Furthermore, additional rolling was performed based on two further rolling schedules with low Z-H parameter values, but different end-of-rolling reduction values. These schedules were carried out in order to explore how the quantity of cube texture saved after deformation impacts its growth during subsequent annealing.

In all schedules, the ingots cast by the tested alloy technology were analyzed using the standard method. The ingots were broken down in a hot reversing mill and then rolled in the four-stand continuous mill, according to the schedules described in Table 3. In the modes 1 and 2, after reaching steady-state conditions, the mill was stopped and the metal cooled rapidly. Samples were collected before and after each stand. In order to study the microstructure and texture of the metal after self-annealing, additional hot rolling based on schedules 1 and 2 was performed without rapid cooling. In this case, the metal was involved in a coil and slowly cooled, maintaining its temperature higher than the recrystallization limit for several hours. In schedules 3 and 4, rolling was conducted without instant stopping and cooling, with samples collected after self-annealing in a coil during cooling. In all cases, the samples were cut only from the central layers in order to exclude the influence of friction, and then sent for X-ray and optical microscopy analysis of texture.

In all cases, the survey plane was parallel to the rolling plane. The textures were studied via the backscatter method using a DRON−7 X-ray diffractometer with Co K_α radiation in the form of four incomplete pole figures {111}, {200}, {220} and {311}. Slope angle α (0−70°) and turn angle β (0−360°) ranges with an increment of α and β of 5° were applied. The

Table 3 Continuous mill rolling schedules

Mode No.	Temperature/°C					True strain		Strain rate				Z-H parameter, Z			
	Entry	T2	T3	T4	Exit	1	4	1	2	3	4	1	2	3	4
1	430	388	361	343	326	0.72	2.76	4.09	11.24	42.60	75.81	1.06×10^{13}	9.83×10^{13}	8.9×10^{14}	3.78×10^{15}
2	410	294	255	232	215	0.72	2.76	1.67	4.44	16.32	32.16	4.94×10^{14}	1.54×10^{16}	2.89×10^{17}	2.09×10^{18}
3	465	420	390	373	346	1.01	2.30	3.11	7.96	23.77	43.44	2.15×10^{12}	1.89×10^{13}	1.2×10^{14}	7.82×10^{14}
4	460	405	375	360	359	1.01	2.76	3.25	8.13	23.87	42.17	4.10×10^{12}	3.73×10^{13}	2.19×10^{14}	6.24×10^{14}

intensity drop at the periphery of the pole figure due to the defocusing effect was compensated by the correction factors calculated taking account the conditions of the X-ray pole figures photograph in accordance with Refs. [49,50]. The orientation distribution function was then calculated for the measured pole figures, presented as superposition of a large number (2000) of standard distributions with identical low scattering. The standard function centers were arranged in a regular 3D-orientation space, with the same orientation distribution function (ODF) used to calculate complete pole figures and inverse pole figures for three mutually perpendicular sample directions: normal to the rolling plane, rolling direction and transverse direction. For convenience of working with the ODFs, the three-dimensional function was approximated as a sum of several standard functions (textural components, ideal orientations with a certain spread):

$$f(g)=\sum_{i=1}^{N}W_i f^{\mathrm{s}}(g,g_i,\varepsilon_i) \tag{4}$$

where N is the number of standard functions, W_i is volume fraction of i-function, g_i is its center position, and ε_i is scattering parameter.

The set of these textural components was chosen based on the analysis of sections of the ODFs calculated from experimental pole figures. The newly developed file of orientations, including three Euler angles and the preliminary parameters W_i and ε_i, was processed using an approach proposed in Ref. [51]. The orientation scatter magnitude ε_i for the ODF model was chosen for each orientation separately in accordance with its scatter region in the experimental ODF. As a criterion for the adequacy of the orientation choice, we chose the minimum of the root-mean-square deviation between the ODF restored from the pole figures and the ODF represented by the sum of single orientations.

The microstructure was also analyzed using an Axiovert−40 MAT optical microscope.

3 Results

Figure 3 illustrates 8011 alloy microstructure transformation during hot rolling in the continuous mill.

Comparative analysis of the two microstructures reveals a number of patterns. A fully recrystallized structure can be observed between the first and second passes for schedule No. 1, whereas only a partially recrystallized structure can be observed for schedule No. 2, with the middle layer structure deformed after the second and following passes. In addition, the termination of the recrystallization process is associated with two different factors. First, at high rolling speed, recrystallization termination is associated with inter-deformation interval reduction, with previous study [20] reporting that iron-rich alloys require a longer recrystallization time compared to 3xxx series alloys. Second, an increase in rolling speed will inevitably stimulate the recovery process, thereby competing with and retarding recrystallization. In the case of low rolling speeds, the inter-deformation interval time increases and the temperature decreases, significantly slowing down the metal recrystallization. However, in both cases, surface layers are recrystallized during the intervals. This is caused by the high amount of energy stored in such layers, which enables almost instant recrystallization initiation even at low temperatures. Also, the characteristic drop in temperature due to contact with the cooled rolls and the rapid re-increase in temperature immediately after the rolling step will have an effect.

After self-annealing in all modes with the exception of schedule No. 2 (characterized by high Z-H parameter values), the recrystallization structure depicted in Fig. 4 was observed.

The texture evolutions of the samples collected from the slab in stand 1 and 4 before and after reduction in high and low speed rolling, respectively, and based on ODF data are presented in Figs. 5−9.

The initial two rolling schedules were conducted at two different rolling speeds: 1) high-speed mode, sufficient to maintain high temperatures and, hence, low Z-H parameter values, and 2) low-speed mode, providing lower strip temperature.

The transformation of the main texture components (rolling texture: β-fiber, and recrystallization texture: cube) is shown in Fig. 10. At sufficiently high rolling temperature, recrystallization occurs partially during inter-stand intervals, with full recrystallization taking place during coil self-annealing. The correlation between the cube volume fractions in the slab and in the self-annealed coil can be observed in Fig. 10(a). At temperatures below the critical level (schedule 2), the cooled coil retains a deformed structure with prevailing β-fiber orientations. It can be seen clearly in Fig. 10(b) that at the same strain value, the cube texture fraction recorded during deformation is significantly reduced at higher Z-H parameter values. This finding correlates well with the hypothesis reported in Refs. [21,52] that recrystallization texture with predominant cube orientation is formed via the growth of nuclei occurring in areas inheriting such orientation after deformation. Such areas exist due to the stability of cube orientation under symmetric deformation conditions, which is typical of strip middle layers during flat rolling. During recrystallization, the rapid growth in cube orientation nuclei is caused by high mobility of their boundaries separating the cube orientations from the β-fiber orientations. Therefore, in the case of complete recrystallization, the cube texture volume fraction in the self-annealed coil is determined by the cube texture volume fraction in the slab.

Thus, in addition to the effect of fine particle described earlier, the volume of cube texture preserved is also affected by inter-stand and final recrystallization. In

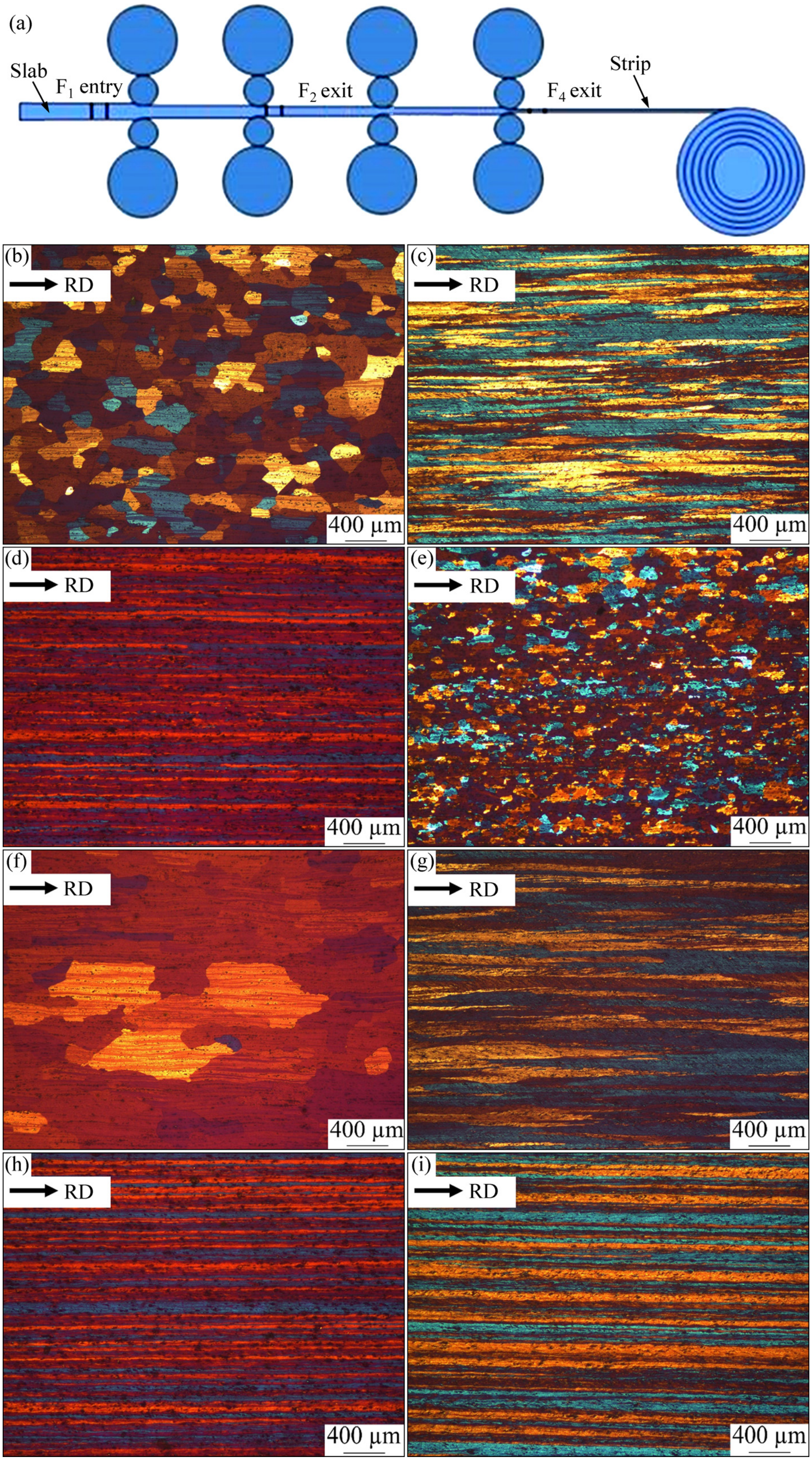

Fig. 3 Microstructure transformation during hot rolling in a continuous mill (a); Schedule No. 1: (b) F_1 entry, (c) F_2 exit, (d) F_4 exit, (e) self-annealing into coil; Schedule No. 2: (f) F_1 entry, (g) F_2 exit, (h) F_4 exit, (i) Self-annealing into coil

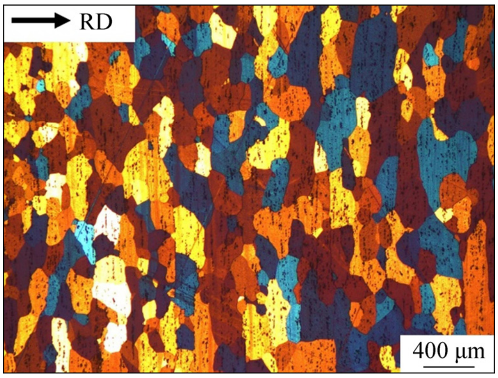

Fig. 4 Coil microstructure after recrystallisation during air cooling (after laboratory milling)

this case, the Z-H parameter has a mixed effect on cube texture in iron-rich alloys. On one hand, increased parameter values will decrease the probability of cube texture formation due to overall reduction in the nuclei fraction. On the other hand, high parameter values lead to increased fine particle rate, which promotes cube texture growth by blocking the nucleation of the other components.

Figure 11 shows ODF data for samples collected from two coils rolled at identical temperatures and rolling speeds but different final pass strain values, as per schedule No. 3 and 4.

In the case of higher strain values, the cube texture is less preserved, with consequently fewer sources for its formation during final recrystallization. This was confirmed by an X-ray structural analysis, which clearly demonstrated a decrease in the cube texture volume fraction after self-annealing at high end-of-rolling reduction values. It should be noted that a sharp cube texture was observed in all tests, except rolling under high Z-H parameter values, providing direct evidence of the second-phase fine particle effect during recrystallization. This finding demonstrates that for mathematical models describing texture evolution as a function of aluminum alloy and thermomechanical treatment, *β*-fiber texture growth should be carefully accounted for by the application of advanced texture

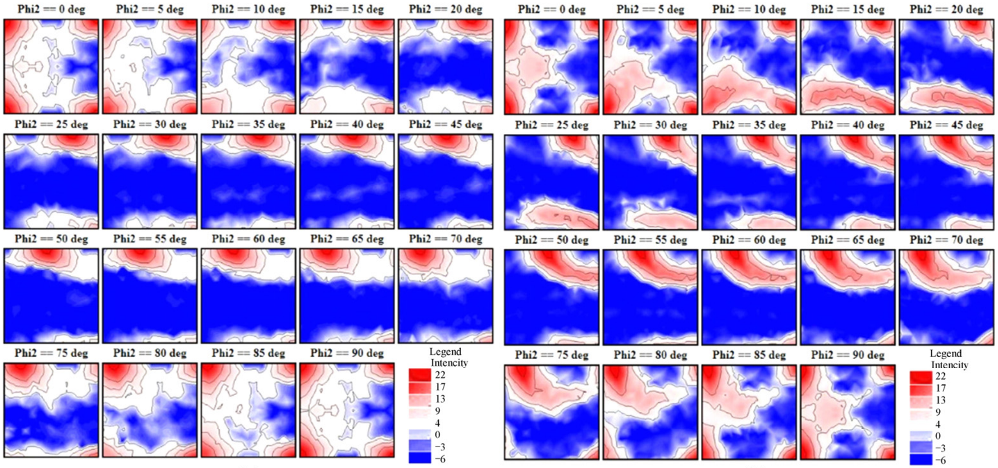

(a) (b)

Fig. 5 ODF of samples collected from slab in stand 1 with high-speed rolling: (a) Before reduction; (b) After reduction

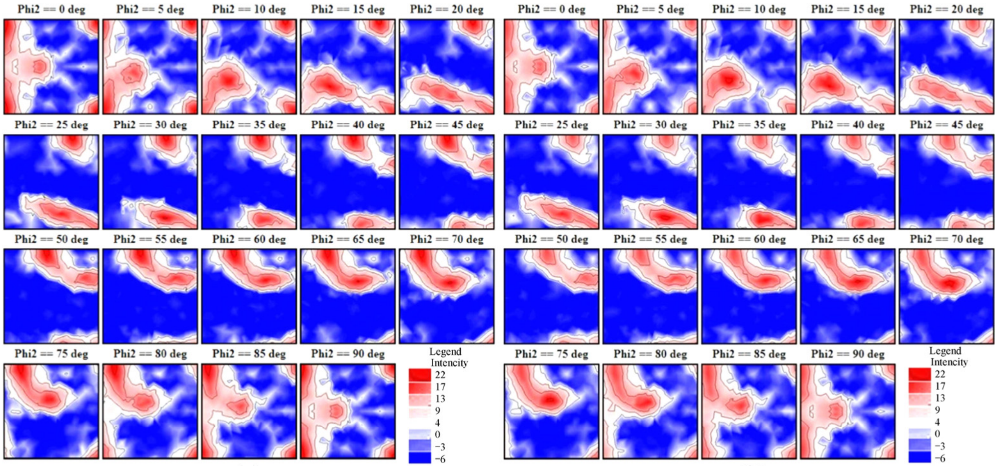

(a) (b)

Fig. 6 ODF of samples collected from slab in stand 4 with high-speed rolling: (a) Before reduction; (b) After reduction

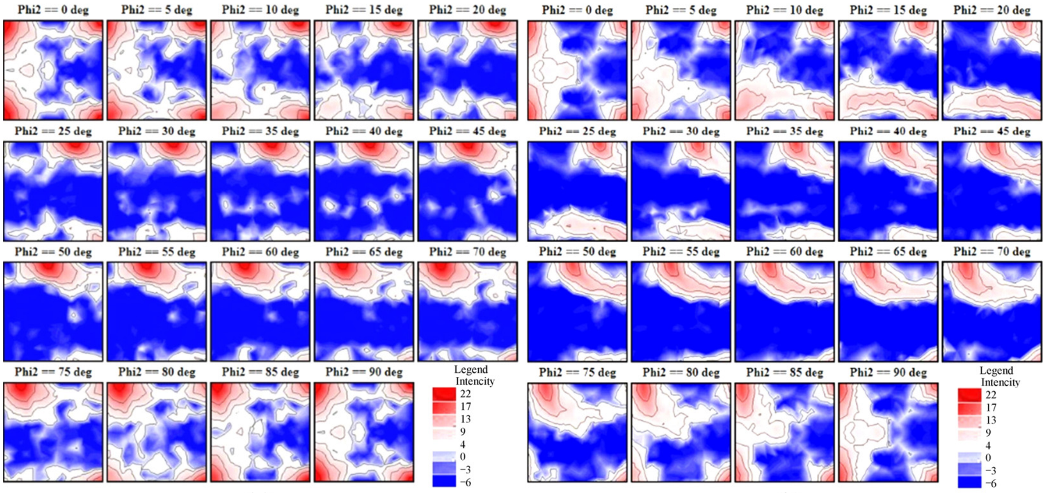

(a) (b)

Fig. 7 ODF of samples collected from slab in stand 1 with low-speed rolling: (a) Before reduction; (b) After reduction

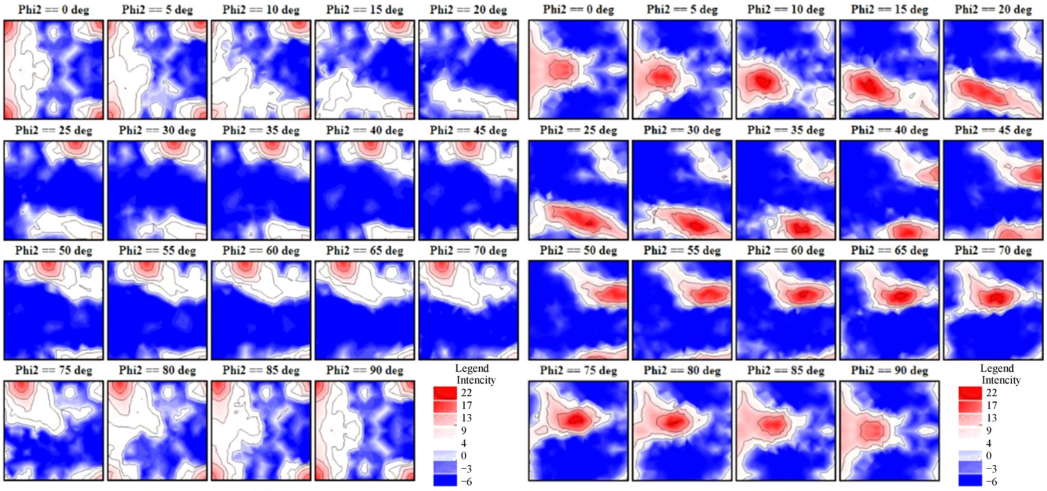

(a) (b)

Fig. 8 ODF of coil after self-annealing: (a) High-speed rolling, above critical temperature; (b) Low speed-rolling, below critical temperature

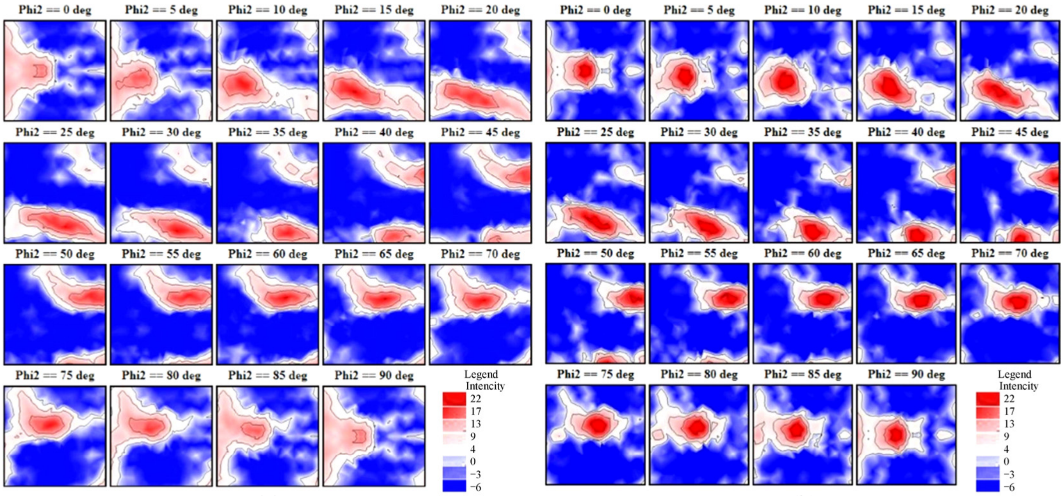

(a) (b)

Fig. 9 ODF of samples collected from slab in stand 4 with low-speed rolling: (a) Before reduction; (b) After reduction

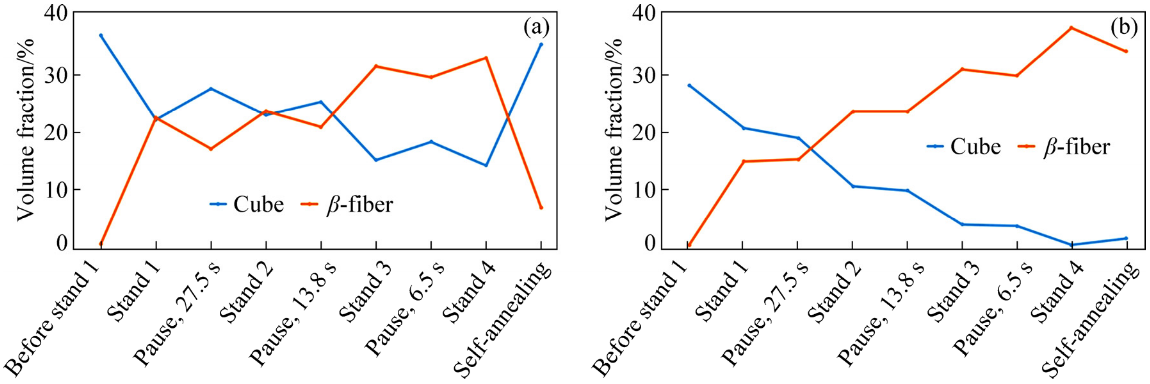

Fig. 10 Texture component transformation during strip rolling at high (a) and low (b) speed

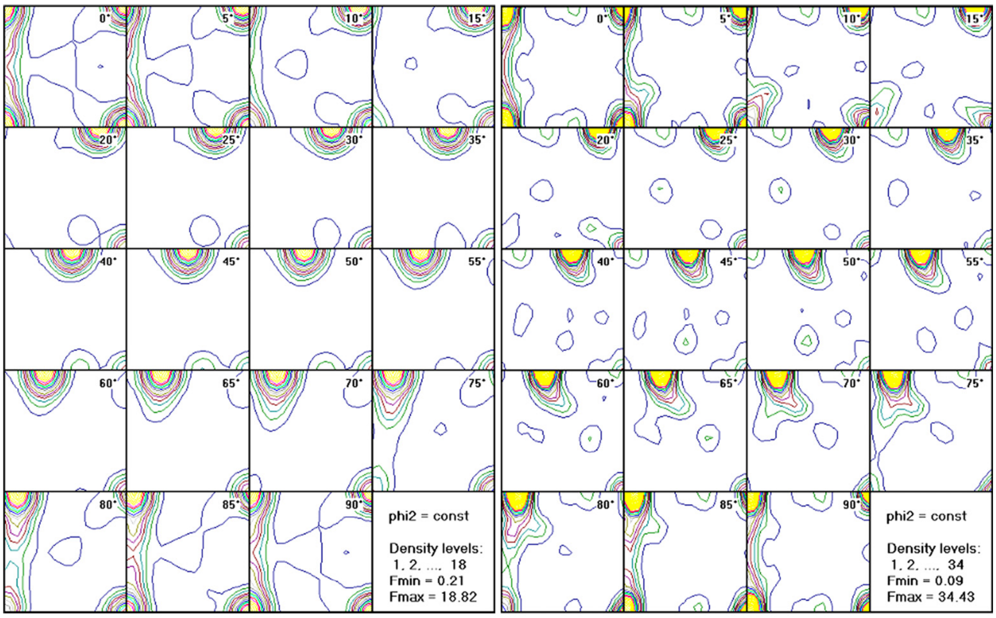

(a) (b)

Fig. 11 ODF of samples collected from fully-recrystallised coils with different slab cube fractions: (a) Schedule 3; (b) Schedule 4

simulation (e.g., LAMEL or GIA) [53−55]. In addition, second-phase fine particle precipitation from supersaturated solutions and their interaction with grain boundaries described as Zener drag should be also calculated with the maximum accuracy.

Figure 12 shows the structure observed in specimens rolled in the laboratory mill under different Z-H parameter values.

Analysis of Fig. 12 reveals almost identical deformed state with almost identical grain sizes for all three modes. Such similarity can be explained by similarity in the Z-H parameter when deformation is followed by recrystallization. In the present study, specimen structures were frozen after rolling, resulting in similar visible patterns. The Z-H parameter effect on deformed structures can be observed both at subgrain level and in differences in crystalline orientations. The samples were rolled once again with water quenching carried out after 20 min recrystallization and annealing at 400 °C for additional microstructural analysis. The results of structural analysis, carried out after annealing, are presented in Fig. 13.

Analysis of Fig. 13 reveals the significant impact of the Z-H parameter (especially at high values) on the grain size, due to the associated increase in recrystallization nuclei (mainly via PSN at deformed grain boundaries). Images obtained from the EBSD orientation analysis are presented in Figs. 14−16. Here, the low-angle (i.e. subgrain) boundaries are shown as white lines occurring in various manner inside the different grain orientations, visible as unique colors.

The detailed analysis of the images presented in Figs. 14−16 leads to the following conclusions:

1) Considerable non-uniformity of low-angle boundary density (expressed as the cumulative low-angle boundary area relative to the enclosed volume), and, therefore, subgrain sizes, can be observed both between individual crystals and within a single grain.

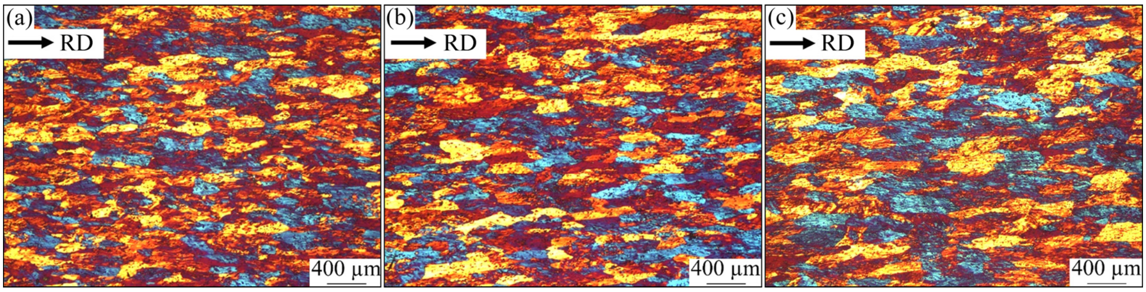

Fig. 12 Microstructures of specimen obtained after deformation under different Z-H parameter values: (a) Z=1.03×10^{12}; (b) Z=3.44×10^{13}; (c) Z=1.6×10^{16}

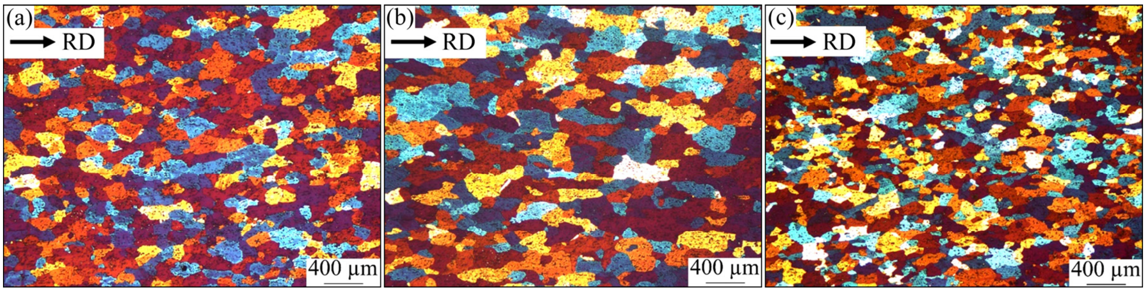

Fig. 13 Microstructures of specimen obtained after annealing and deformation under different Z-H parameter values: (a) Z=1.03×10^{12}; (b) Z=3.44×10^{13}; (c) Z=1.6×10^{16}

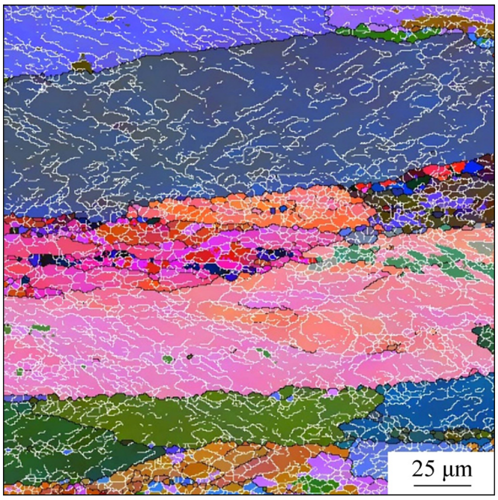

Fig. 14 EBSD image of sample No. 4 (Z=1.03×10^{12}, low Z-H parameter value)

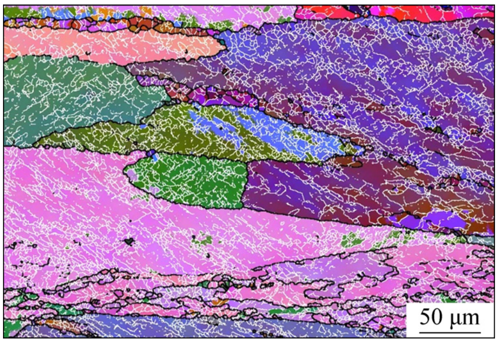

Fig. 15 EBSD image of sample No. 5 (Z=3.44×10^{13}, medium Z-H parameter value)

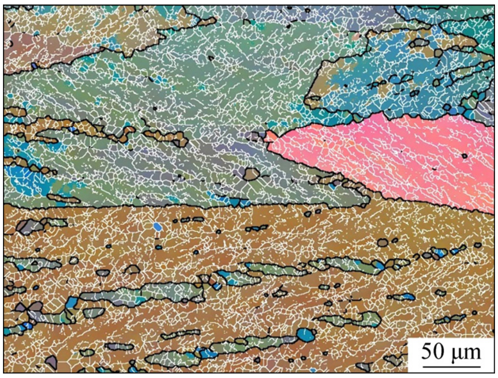

Fig. 16 EBSD image of sample No. 6 (Z=1.6×10^{16}, high Z-H parameter value)

2) This non-uniformity depends on grain orientation. Figure 17 shows the orientations of the grains as depicted in Fig. 16 as {111} pole figure, indicating the plane poles (111), (1$\bar{1}$1) and (1$\bar{1}\bar{1}$) to determine the crystalline orientation. Traces of the normal plane in the pole figure are connected by lines to the respective grains in the EBSD image. Grains 1 and 2 exhibit considerably different orientations, at (158)[13$\bar{2}$] and (23$\bar{2}$)[$\bar{2}$14], respectively, which, in turn, indicates the variation in low-angle boundary density.

3) The subgrain size depends on the crystal size, which is especially evident considering the fine grains located between grains 1 and 2 in Fig. 17.

4) The high-angle boundary density increases close to grain boundaries and second-phase inclusions.

5) The subgrain misorientation angle increases at

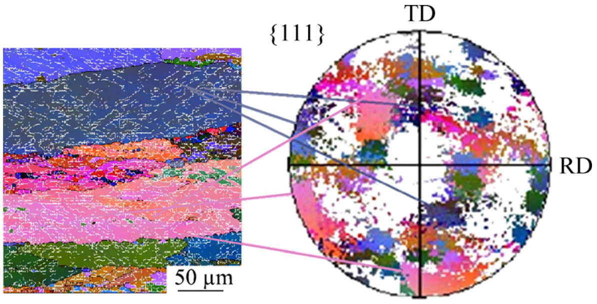

Fig. 17 Grain orientations and plane traces in pole figure

the boundaries of grains with different orientations, resulting in the formation of fine grains as deformation progresses (Fig. 18, fine grains between grains 1 and 2).

The data presented in Figs. 14−16 were subsequently used to evaluate specimen subgrain sizes based on 50 μm × 50 μm zones of maximum and minimum density values, as shown in Figs. 18−20. Thus, the number of subgrains was determined for each zonal area of 2500 μm^2, with the average area of a single subgrain calculated and the typical subgrain size equal to the square root of the average area. The results of these calculations are presented in Fig. 21 as the mean values of the subgrain maximum and minimum size. Figure 21 also contains the data obtained for 3004 alloy, based on the research from Ref. [25] and for 1100 alloy reported in Ref. [56]. The analysis of Fig. 21 and its comparison with other alloys reveals that the subgrain sizes obtained in the present study are much larger than those reported in the other two studies. This can be explained by the fact that the 8011 alloy plates sampled here for strip preparation possessed exceptionally large grains (over 200 μm), whereas 3004 alloy strip typically used for deep drawn and ironed can body production is subjected to preheating and homogenization, causing the formation of a large number of fine phases, inhibiting major grain growth. Nevertheless, all three cases presented in Fig. 21 exhibit a similar trend, confirming the clear dependence of subgrain size on the Zener-Hollomon parameter.

As mentioned in the introduction, Eq. (1) is widely considered as the most universally-accepted expression for the relationship between subgrain size and the Z-H parameter. In this regard, the study reported in Ref. [56] recommends values of m=1, A=−0.196 and B=0.0153 for 1100 alloy, with the current study establishing values of

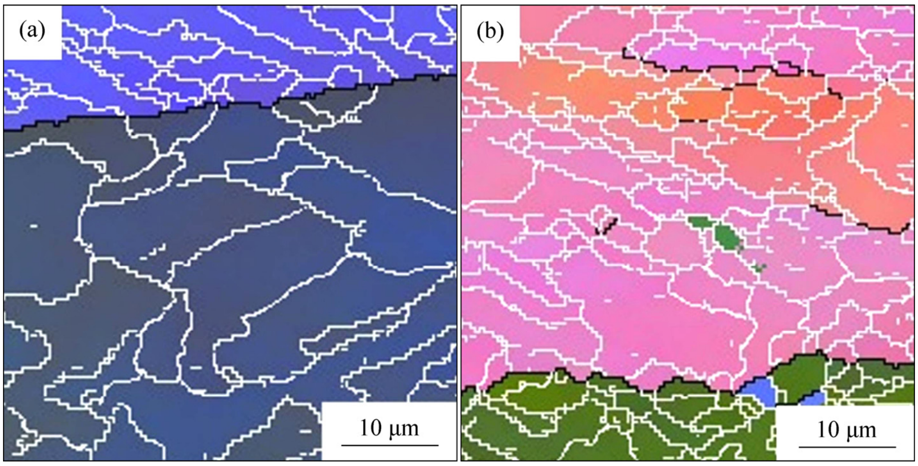

Fig. 18 Subgrain sizes in minimum (a) and maximum (b) low-angle boundary density zones (Sample 4, Z=1.03×10^{12})

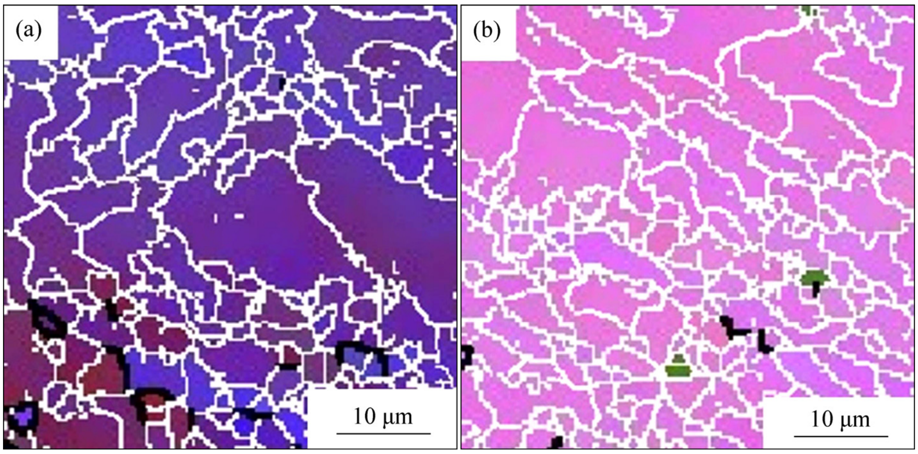

Fig. 19 Subgrain sizes in minimum (a) and maximum (b) low-angle boundary density zones (Sample 5, Z=3.44×10^{13})

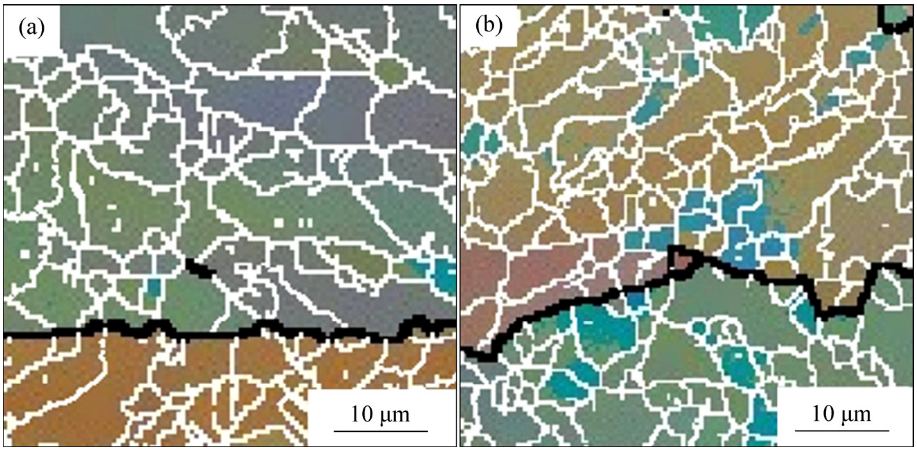

Fig. 20 Subgrain sizes in minimum (a) and maximum (b) low-angle boundary density zones (Sample 6, Z=1.6×10^{16})

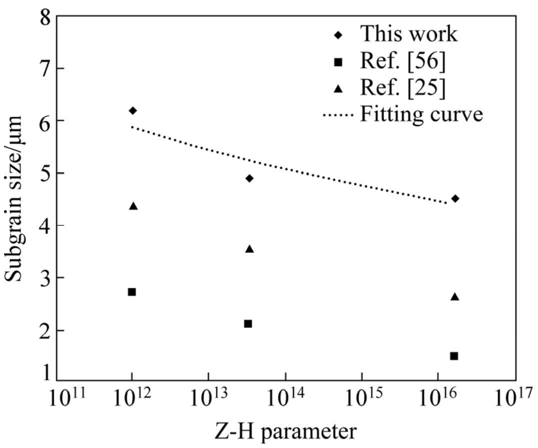

Fig. 21 Subgrain size dependence on Z-H parameter for various alloys

m=1, A=0.00768 and B=0.00588 for the 8011 alloy investigated.

The present study has clearly confirmed the negative linear relationship between subgrain size and the Z-H parameter, with Eq. (1), previously applied to 3xxx and 1xxx series alloys, also applicable to the iron-rich aluminum alloys investigated here.

4 Conclusions

(1) Analysis of the Z-H parameter effect on the main textural components of 8011 alloy during hot rolling revealed that, in addition to fine second-phase particles, the cube orientation micro-volume fraction inherited after deformation has an effect on the texture composition as it has been previously observed in 1xxx and 3xxx series alloys.

(2) An increase in Z-H parameter values leads to a decrease in the residual cube texture, with the greater impact on 8xxx iron-rich alloys than on 1xxx and 3xxx series alloys. The high Z-H parameter value not only stimulates a reduction in the cube texture fraction but also facilitates second-phase particle precipitation, suppressing PSN-based nuclei growth during recrystallization. This finding proves the need for the application of texture simulation (e.g. GIA or ALAMEL-type) models simulating deformation texture formation, as well as the introduction of new models describing the commutation of second-phase particle precipitation kinetics and their interaction with grain boundaries.

(3) The EBSD analysis reveals that substructure formation and its dependence on the Z-H parameter are similar to those observed in 3xxx and 1xxx series alloys; this relationship can thus be described using the same models for each group of alloys.

Acknowledgments

This work was funded by a grant of the Russian Science Foundation (Project 18-79-10099).

References

[1] HIRSCH J. Aluminium in innovative light-weight car design [J]. Materials Transactions, 2011, 52: 818−824.

[2] LAMBERTI M, ESCHER F. Aluminium foil as a food packaging material in comparison with other materials [J]. Food Reviews International, 2007, 23: 407−433.

[3] MILLER W, ZHUANG L, BOTTEMA J, WITTEBROOD A, de SMET P, HASZLER A, VIEREGGE A. Recent development in aluminium alloys for the automotive industry [J]. Materials Science and Engineering A, 2000, 280: 37−49.

[4] RAMBABU P, PRASAD N E, KUTUMBARAO V V, WANHILL R J H. Aluminium alloys for aerospace applications [C]//Aerospace Materials and Material Technologies: Aerospace Materials. Singapore: Springer, 2017: 29−52.

[5] HOLGER A, AEGERTER J, ENGLER O. Analysis of earing in deep drawn cups [C]//AIP Conference Proceedings. Melville, USA: AIP Publishing Center, 2010: 417−424.

[6] HIRSCH J. Texture evolution and earing in aluminium can sheet [J]. Materials Science Forum, 2005, 495−497: 1565−1572.

[7] ENGLER O. Modeling of texture and texture-related properties during the thermo-mechanical processing of aluminum sheets [J]. Materials Science Forum, 2003, 426: 3655−3660.

[8] HUTCHINSON W B, OSCARSSON A, KARLSSON Å. Control of microstructure and earing behaviour in aluminium alloy AA 3004 hot bands [J]. Materials Science and Technology, 1989, 5(11): 1118−1127.

[9] VATNE H E, ØRSUND R, MARTHINSEN K, NES E. Modeling recrystallization kinetics, grain sizes, and textures during multipass hot rolling [J]. Metallurgical and Materials Transactions A, 1996, 27(12): 4133−4144.

[10] VATNE H E, PEROCHEAU F, EKSTRÖM H E, POIZAT L, NORD-VARHAUG K, MARTHINSEN K, LINDH E, HAGSTRÖM J, FURU T. Industrial verification of microstructural models for thermomechanical processing by application to hot rolling of AA3104 [J]. Materials Science Forum, 2000, 331−337: 551−556.

[11] VATNE H E, NES E. A model for recrystallisation kinetics, texture and grain size applied to multipass hot rolling of an AlMgMn aluminium alloy [J]. Computational Materials Science, 1996, 7: 5−10.

[12] WELLS M A, SAMARASEKERA I V, BRIMACOMBE J K, HAWBOLT E B, LLOYD D J. Modeling the microstructural changes during hot tandem rolling of AA5XXX aluminum alloys: Part I. Microstructural evolution [J]. Metallurgical and Materials Transactions B, 1998, 29(3): 611−620.

[13] WELLS M A, SAMARASEKERA I V, BRIMACOMBE J K, HAWBOLT E B, LLOYD D J. Modeling the microstructural changes during hot tandem rolling of AA5XXX aluminum alloys: Part III. Overall model development and validation [J]. Metallurgical and Materials Transactions B, 1998, 29(3): 709−719.

[14] WELLS M A, MAIJER D M, JUPP S, LOCKHART G, van der WINDEN M R. Mathematical model of deformation and microstructural evolution during hot rolling of aluminium alloy 5083 [J]. Materials Science and Technology, 2003, 19(4): 467−476.

[15] ARYSHENSKII E, KAWALLA R, HIRSCH J. Development of new fast algorithms for calculation of texture evolution during hot continuous rolling of Al−Fe alloys [J]. Steel Research International, 2017, DOI: 10.1002/srin.201700053.

[16] SCHÄFER C, POMANA G, MOHLES V, GOTTSTEIN G, ENGLER O, HIRSCH J. Recrystallization modeling of AA8XXX alloys with cellular automata considering recovering kinetics [J]. Advanced Engineering Materials, 2010, 12(3): 131−140.

[17] ARYSHENSKII E V, SEREBRYANY V N, TEPTEREV M S, GRECHNIKOVA A F. Study of the laws of texture formation in the alloy 8011 during cold rolling and annealing [J]. The Physics of Metals and Metallography, 2015, 116(9): 925−931.

[18] ENGLER O. On the influence of dispersoids on the particle stimulated nucleation of recrystallization in an Al−Fe−Si model alloy [J]. Materials Science Forum, 1998, 275: 483−488.

[19] EVGENII A, KAWALLA R, VLADIMIR A, CHRISTIAN S. Investigation of texture and structure evolution during hot rolling of 1070, 3104 and 8011 aluminum alloys in continuous mill [J]. La Metallurgia Italiana, 2017(3): 11−21.

[20] VELMANIRAJAN K, ANURADHA K, THAHEER A S A, NARAYANASAMY R, MADHAVAN R, SUWAS S. Experimental investigation of forming limit, void coalescence and crystallographic textures of aluminum alloy 8011 sheet annealed at various temperatures [J]. Archives of Civil and Mechanical Engineering, 2014, 14(3): 398−416.

[21] DALLAND O, NES E. Origin of cube texture during hot rolling of commercial Al−Mn−Mg alloys [J]. Acta Materialia, 1996, 44(4): 1389−1411.

[22] VATNE H E, NES E, DAALAND O. On the formation of cube texture in aluminium [J]. Materials Science Forum, 1994, 157: 1087−1094.

[23] VATNE H E, FURU T, ØRSUND R, NES E. Modelling recrystallization after hot deformation of aluminium [J]. Acta Materialia, 1996, 44(11): 4463−4473.

[24] CASTRO-FERNANDEZ F R, SELLARS C M, WHITEMAN J A. Changes of flow stress and microstructure during hot deformation of Al−1Mg−1Mn [J]. Materials Science and Technology, 1990, 6(5): 453−460.

[25] DUAN X, SHEPPARD T. Influence of forming parameters on the final subgrain size during hot rolling of aluminium alloys [J]. Journal of Materials Processing Technology, 2002, 130: 245−249.

[26] SELLARS C M, TEGART W J M. Hot workability [J]. International Metallurgical Reviews, 1972, 17(1): 1−24.

[27] DUAN X, SHEPPARD T. Prediction of temperature evolution by FEM during multi-pass hot flat rolling of aluminium alloys [J]. Modelling and Simulation in Materials Science and Engineering, 2001, 9(6): 525−538.

[28] ZHANG X M, XU M, TANG J G, OU J. Hot-compression behavior of Al−1Mn−1Mg alloy [J]. Journal of Central South University of Technology, 2010, 17(3): 425−430.

[29] DUAN X, SHEPPARD T. Simulation of substructural strengthening in hot flat rolling [J]. Journal of Materials Processing Technology, 2002, 125: 179−187.

[30] ZAIDI M A, SHEPPARD T. Development of microstructure throughout roll gap during rolling of aluminium alloys [J]. Metal Science, 1982, 16(5): 229−238.

[31] NES E. Constitutive laws for steady state deformation of metals, a microstructural model [J]. Scripta Metallurgica et Materialia, 1995, 33(2): 225−231.

[32] COPREAUX J, LANTERI S, SCHMITT J H. Effect of precipitation on the development of dislocation substructure in low carbon steels during cold deformation [J]. Materials Science and Engineering A, 1993, 164(1−2): 201−205.

[33] MATHEW M D, SUNDARARAMAN M, MANNAN S L. Dislocation substructure and precipitation in Type 316 stainless steel deformed in creep [J]. Materials Transactions, JIM, 1997, 38(1): 37−42.

[34] ROUMINA R, SINCLAIR C W. Recovery kinetics in the presence of precipitates: The softening response of an Al−Mg−Sc alloy [J]. Acta Materialia, 2010, 58(1): 111−121.

[35] VERDIER M, BRECHET Y, GUYOT P. Recovery of Al−Mg alloys: Flow stress and strain-hardening properties [J]. Acta Materialia, 1998, 47(1): 127−134.

[36] YOSHIDA H, OOKUBO Y. Effect of precipitation of impurities during annealing on the rate of recovery and recrystallization in 1050 aluminum hot-rolled sheets [J]. Materials Transactions, 2015, 569(12): 1960−1967.

[37] KUMAR N, JAYAGANTHAN R, BROKMEIER H G. Effect of deformation temperature on precipitation, microstructural evolution, mechanical and corrosion behavior of 6082 Al alloy [J]. Transactions of Nonferrous Metals Society of China, 2017, 27(3): 475−492.

[38] CRUMBACH M, GOTTSTEIN G. Analysis of the activity of {110}⟨110⟩ slip in AA3103 by inverse modeling [J]. Materials Science and Engineering A, 2004, 387−389(1): 282−287.

[39] HUANG Y, HUMPHREYS F J, FERRY M. Hot deformation and annealing of cube oriented aluminium single crystals [J]. Materials Science and Technology, 2000, 16(11−12): 1367−1371.

[40] VATNE H E, SHAHANI R, NES E. Deformation of cube-oriented grains and formation of recrystallized cube grains in a hot deformed commercial AlMgMn aluminium alloy [J]. Acta Materialia, 1996, 44(11): 4447−4462.

[41] JONES M, HUMPHREYS F. Interaction of recrystallization and precipitation: The effect of Al3Sc on the recrystallization behaviour of deformed aluminium [J]. Acta Materialia, 2003, 51(8): 2149−2159.

[42] LIU J, TAO B, LI S, LI M. Evolution of microstructure and precipitates with cycle annealing temperature of an Al−6Mg−

Mn−Sc−Zr alloy [J]. Materials and Manufacturing Processes, 2007, 22(1): 1−4.

[43] OCENASEK V, SLAMOVA M. Resistance to recrystallization due to Sc and Zr addition to Al−Mg alloys [J]. Materials Characterization, 2001, 47(2): 157−162.

[44] LENTZ M, LAPTYEVA G, ENGLER O. Characterization of second-phase particles in two aluminium foil alloys [J]. Journal of Alloys and Compounds, 2016, 660: 276−288.

[45] ENGLER O, VATNE H E. Modeling the recrystallization textures of aluminum alloys after hot deformation [J]. JOM, 1998, 50(6): 23−27.

[46] RUSHCHITS S V, ARYSHENSKY E V, SOSEDKOV S M, AKHMED'YANOV A M. Modeling the hot deformation behavior of 1565ch aluminum alloy [J]. Key Engineering Materials, 2016, 684: 35−41.

[47] RØYSET J, RYUM N. Scandium in aluminium alloys [J]. International Materials Reviews, 2005, 50(1): 19−44.

[48] ZAKHAROV V V. Combined alloying of aluminum alloys with scandium and zirconium [J]. Metal Science and Heat Treatment, 2014, 56(5): 281−286.

[49] SEREBRYANY V, KURTASOV S F, SAVYOLOVA T I. Pole figure measurement plan influence on accuracy ODF coefficients determined by modified harmonic method [J]. Materials Science Forum, 2005, 495−497: 1693-0.

[50] IVANOVA T M, LUBMAN H U, SAVYOLOVA T I, SEREBRYANY V. The influence of errors of X-ray texture measurements on ODF calculation with central normal distribution approximation [J]. Materials Science Forum, 2005, 495−497: 273−276.

[51] SAVYOLOVA T I, KOURTASOV S F. ODF restoration by orientations grid [J]. Materials Science Forum, 2005, 495−497: 301−306.

[52] VATNE H E, ENGLER O, NES E. Effect of precipitates on texture development [J]. Materials Science Forum, 1994, 157(6): 1501−1506.

[53] ENGLER O, CRUMBACH M, LI S. Alloy-dependent rolling texture simulation of aluminium alloys with a grain-interaction model [J]. Acta Materialia, 2005, 53(8): 2241−2257.

[54] van HOUTTE P, DELANNAY L, SAMAJDAR I. Quantitative prediction of cold rolling textures in low-carbon steel by means of the Lamel model [J]. Textures and Microstructures, 1999, 31(3): 109−149.

[55] van HOUTTE P, LI S, SEEFELDT M, DELANNAY L. Deformation texture prediction: From the Taylor model to the advanced Lamel model [J]. International Journal of Plasticity, 2005, 21(3): 589−624.

[56] VATNE H E. Modeling recrystallization in multi-pass hot rolling and extrusion of commercial aluminum alloys [C]//Deformation of Aluminum Alloys II, Proceedings of the Second Symposium. Rosemont, Illinois, USA: TMS, 1998: 24−36.

Zener-Hollomon 参数对含铁锻造铝合金热变形处理过程中亚结构和织构演变的影响

Evgenii ARYSHENSKII[1,2], Jürgen HIRSCH[2,3], Vladimir BAZHIN[4], Rudolf KAWALLA[1], Ulrich PRAL[1]

1. TU Bergakademie Freiberg, Institut für Metallformung, Bernhard-von-Cotta-Str. 4, 09599 Freiberg, Germany;
2. Samara State Aerospace University, Samara National Research University,
MoskovskoyeShosse 34, 443086 Samara, Russia;
3. Hydro Aluminium Rolled Products GmbH, Research and Development, D-53117 Bonn, Germany;
4. St. Petersburg Mining University, Institute of Automation of Manufacturing Processes,
2, 21st Line, St Petersburg 199106, Russia

摘　要：研究 Zener-Hollomon 参数对含铁锻造铝合金(AA8011)亚结构和织构演变的影响。采用 X 射线织构分析、电子背散射衍射(EBSD)和光学显微镜等技术进行表征。结果表明，Zener-Hollomon 参数对含铁铝合金热变形处理过程中立方织构的演变具有显著影响。增大 Zener-Hollomon 参数会减少热变形过程中立方织构的数量，且能加强退火过程中的颗粒诱发形核 (PSN)的能力。然而，低温热变形处理会导致活性沉淀，这些细而分散的颗粒会阻碍除了产生立方大晶粒的晶核外的所有晶核。综上，在含铁锻造铝合金中，Zener-Hollomon 参数与亚晶粒尺寸之间的相关性与在 3xxx 系列合金中观察到的类似，可以用系列推导方程描述。

关键词：铝合金；织构；Zener-Hollomon 参数；亚结构；热轧

(Edited by Bing YANG)